Geochemistry, Geophysics, Geosystems

RESEARCH ARTICLE
10.1029/2018GC007738

Anisotropic Physical Properties of Mafic and Ultramafic Rocks From an Oceanic Core Complex

G. Bayrakci[1], I. H. Falcon-Suarez[2], T. A. Minshull[1], L. North[2], A. Barker[1], B. Zihlmann[1], S. Rouméjon[3,4], and A. I. Best[2]

[1]Ocean and Earth Science, National Oceanography Centre Southampton, University of Southampton, Southampton, UK, [2]National Oceanography Centre, University of Southampton, Southampton, UK, [3]Institute of Geochemistry and Petrology, ETH Zürich, Zürich, Switzerland, [4]Institut de Physique du Globe de Paris, Sorbonne Paris Cité, Paris, France

Key Points:
- In the absence of major surface conduction, the electrical resistivity and the permeability of mafic and ultramafic rocks are correlated
- Both rock types show anisotropy in electrical resistivity, with one high and two similar low-resistivity axes, indicating foliation
- The difference in the direction of electrical high resistivity axes of mafic and ultramafic rocks may aid their identification by remote geophysical methods

Correspondence to:
G. Bayrakci,
g.bayrakci@soton.ac.uk

Citation:
Bayrakci, G., Falcon-Suarez, I. H., Minshull, T. A., North, L., Barker, A., Zihlmann, B., et al. (2018). Anisotropic physical properties of mafic and ultramafic rocks from an oceanic core complex. *Geochemistry, Geophysics, Geosystems*, *19*, 4366–4384. https://doi.org/10.1029/2018GC007738

Received 7 JUN 2018
Accepted 18 OCT 2018
Accepted article online 24 OCT 2018
Published online 8 NOV 2018

Abstract We analyzed the physical properties of altered mafic and ultramafic rocks drilled at the Atlantis Massif (Mid-Atlantic Ridge, 30°N; Integrated Ocean Discovery Program Expeditions 304-305 and 357). Our objective was to find a physical property that allows direct distinction between these lithologies using remote geophysical methods. Our data set includes the density, the porosity, *P* and *S* wave velocities, the electrical resistivity, and the permeability of mafic and ultramafic samples under shallow subsurface conditions (confining pressure up to 50 MPa equivalent to ~2-km depth). In shallow subsurface conditions, mafic and ultramafic samples showed distinct differences in the density, the seismic wave velocities, and the electrical resistivity (mafic samples: 2,840 to 2,860 kg/m^3, 5.92 to 6.70 km/s, and 60 to 221 Ω m; ultramafic samples: 2,370 to 2,790 kg/m^3, 3.36 and 3.62 km/s, and 8 to 44 Ω m). However, we observed an overlap between physical properties of mafic and ultramafic rocks when we compared our measurements with those acquired from similar environments. The anisotropic homogeneous electrical resistivity inversion shows transverse isotropy symmetry, which is typical of a foliated microstructure. In both the inversion results and the thin sections, the direction of high resistivity axes of ultramafic rock samples is systematically perpendicular to the equivalent axes in mafic rock samples analyzed in this study. Our sample scale study suggests that electrical resistivity anisotropy may allow us to distinguish mafic and ultramafic lithologies via controlled source electromagnetic surveys. When surface conduction is negligible, the electrical resistivity can be used as proxy for permeability.

1. Introduction

Altered mantle rock outcrops are commonly observed along slow- and ultraslow-spreading ridges (Bonatti et al., 1971; Cannat et al., 1995; Sauter et al., 2013) as well as in ocean-continent transitions (Minshull, 2009). These mantle rocks are tectonically exhumed along large offset faults (Cannat et al., 2009; Karson & Dick, 1983; Tucholke & Lin, 1994) and host intrusive mafic bodies in variable amounts. For example, gabbros are estimated to account for 30% of the Atlantis Massif southern wall (Mid-Atlantic Ridge 30°N; Blackman et al., 2002), while they account for only 3% along parts of the easternmost Southwest Indian Ridge (62–65°E; Sauter et al., 2013). Intrusive mafic bodies influence the geological processes active in settings where mantle is uplifted: they modify the rheology of the lithosphere exhumed along faults (Boschi et al., 2006); they form an additional source of heat that impacts the rate of cooling at depth; and they potentially control the distribution of fluid pathways in hydrothermal systems (Bird et al., 1988). However, due to the difficulties of sampling at spreading ridges and in ocean-continent transitions, estimating the size and distribution of these mafic bodies remains challenging.

A way to overcome such challenge is the use of geophysical data and the contrast in physical properties between peridotites and gabbros. Although these rocks theoretically present distinct signatures (e.g., density 3,300 vs. 2,750–3,300 kg/m^3 and *P* wave velocity of 8 vs. 5.95–7.6 km/s for peridotites and gabbros, respectively), they are often found altered, which considerably affects their physical properties.

Serpentinization occurs when hydrothermal fluids are brought in contact with olivine and/or orthopyroxene. Serpentinization reactions mainly produce serpentine (lizardite, chrysotile, and/or antigorite) and iron oxides such as magnetite. From a fresh dunite that mainly contains olivine, to a serpentinite in which all the olivine is altered, there is a significant drop in both the density (3,300 to 2,485 kg/m^3) and *P* wave velocity (8 to 4.8 km/s; Carlson & Miller, 2003). Serpentinization may also result in up to 40% of volume increase (Escartín & Cannat, 1999).

In contrast, gabbroic rocks usually show lower variations in physical properties. Depending on their mineralogy and their degree of alteration, the density and *P* wave velocity of mafic rocks range between 2,750 and 3,300 kg/m^3 and 5.95 and 7.6 km/s, respectively (Iturrino et al., 1996). Gabbroic rocks can also contain olivine, though in much lower amounts so that the serpentine remains limited. Instead, alteration of pyroxenes and plagioclases forms other hydrated minerals such as amphibole, chlorite, and talc, which also modify the physical properties of these rocks.

In addition to the degree of alteration, the development of cracks and fractures directly affects the physical properties. When these rocks are brought to near the seabed, the associated stress-release opening of cracks and fractures leads to porosity increase, which in turn affects densities and velocities. Only at in situ pressures above 200 MPa (overburden pressure at ~8 km below seafloor, bsf), where the cracks and fractures are closed, do the wave velocities of these rocks start to increase linearly with pressure (Carlson & Miller, 2004; Christensen, 1966; Iturrino et al., 1991). Above 200 MPa, the densities and velocities of partially serpentinized peridotite overlap with those of mafic rocks when the degree of serpentinization is between 20% and 40%.

Mafic and ultramafic rocks also coexist in shallower ocean crust, at oceanic core complexes (OCCs; Blackman et al., 2011; Escartín et al., 2003) or at rifted portions of fast-spread lithosphere (MacLeod, Boudier, et al., 1996; MacLeod, Célérier, et al., 1996), and at ocean-continent transitions (Bronner et al., 2011; Dean et al., 2000). In shallow subsurface environments, a high degree of alteration is commonly observed due to the easy access of seawater to the exposed magnesium bearing rocks. Evans et al. (2010) showed that the electrical resistivity allows to distinguish mafic and ultramafic rocks near the seabed via the difference in their porosity. In shallow environments, higher porosities and lower densities and velocities might be expected for the fully serpentinized ultramafic rocks. However, the effect of open fractures and cracks (Hyndman & Drury, 1976; Miller & Christensen, 1997), the presence of thick sedimentary cover reducing the access of water to fresh magnesium bearing rocks (Rüpke et al., 2013), and temperature and pressure conditions affecting the degree of serpentinization (Macdonald & Fyfe, 1985) may complicate the distinction between mafic and ultramafic rocks in shallow subsurface.

Due to the nonunique interpretation of sparse seismic data, in Atlantis Massif, the predrilling interpretation of seismic data with apparent high velocities (7.5 km/s) at depth of 600 m bsf and a positive gravity anomaly corresponding to rocks of 200–400 kg/m^3 higher than the surrounding led to the suggestion of a local very shallow Moho beneath the central dome. However, the Integrated Ocean Discovery Program (IODP) Expedition 304-305 recovered 91% mafic rocks from the Site 1309 (1.4 km deep; Blackman et al., 2011, 2006). Similarly, different interpretations of the magmatic content of the ocean-continent transition zone at the Iberia-Newfoundland margin system lead to different interpretation of the origin of J magnetic anomaly, resulting in contradictory inferred ages of mantle exhumation (Bronner et al., 2011; Dean et al., 2000; Sibuet et al., 2007; Tucholke & Sibuet, 2007).

Various physical properties such as *P* and *S* wave velocities, V_p/V_s ratios (Bezacier et al., 2010; Horen et al., 1996), and *P* wave anisotropy (Christensen, 2004; Horen et al., 1996), the density (Carlson & Miller, 2003) and magnetic susceptibility (Toft et al., 1990) have been used to infer the degree of serpentinization of the ultramafic rocks. Although these properties are good indicators, their use to distinguish between mafic and ultramafic rocks is not always successful. Olivine and orthopyroxene display strong deformation-induced preferred orientations and exhibit pronounced *P* wave anisotropy with the fast axis oriented along the lithospheric flow or perpendicular to the principal deformation stress (Christensen, 2004). On the other hand, complete serpentinization results in a mesh texture that usually suppresses this anisotropy. Therefore, the *P* wave anisotropy of partially serpentinized peridotite ranges between 15% for fresh peridotite and 1% for serpentinite (Christensen, 2004; Cole et al., 2002). Mafic rocks exhibit also some *P* wave anisotropy caused by grain rotation, recrystallization in a stress field or in a thermal gradient, or flow orientation and dislocation-controlled slip (Anderson, 2007). Iturrino et al. (1991) report a *P* wave anisotropy of 6% for gabbroic rocks. Although the percentage of the anisotropy of mafic rocks overlaps with the anisotropy range of partially serpentinized peridotites, the directions may differ.

The electrical resistivity (denoted hereafter as resistivity) offers one of the widest ranges of any common physical properties of solids (Guéguen & Palciauskas, 1994). Previous studies on core samples and remote electromagnetic studies have suggested that at shallow subsurface the resistivity of mafic rocks is higher than those of partially serpentinized ultramafic rocks (Evans et al., 2010; Stesky & Brace, 1973). However,

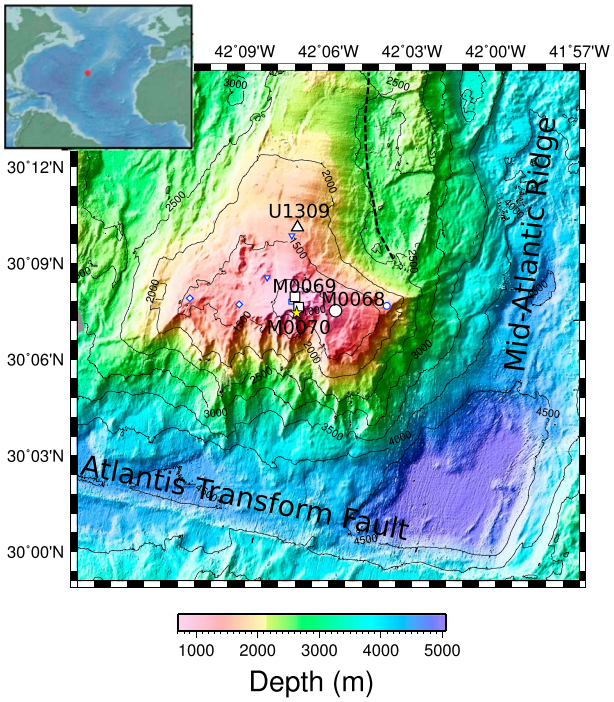

Figure 1. Bathymetric map of the Atlantis Massif oceanic core complex (Früh-Green et al., 2017). The white triangle shows the location of Site U1309 drilled during Integrated Ocean Discovery Program Expedition 304-305. Mafic samples acquired from the Integrated Ocean Discovery Program Holes U1309-B and U1309-D were used in this study. The large white symbols surrounded by black lines show the locations of the Expedition 357 sites used in this study; (circle) eastern Site M0068 and (squares) central Sites M0069 and M0076. Other white symbols surrounded by blue represent the sites drilled during the Expedition 357, which are not used in this study. The yellow star shows the location of Lost City Hydrothermal Field. The black dashed line shows the detachment fault interpreted by Boschi et al. (2006). The exposed detachment surface is roughly represented by the 2,500-m bathymetric contour. Inset shows the location of the Atlantis Massif along the Mid-Atlantic Ridge.

the resistivity values may overlap at deeper environments. The anisotropy of the electrical resistivity is expected to be correlated with the seismic anisotropy (Guo et al., 2011), and it may be more easily detectable than the seismic anisotropy. Here we test the hypothesis that the direction of resistivity anisotropy may be different for mafic and ultramafic rocks and may allow to distinguish them in the future by controlled source electromagnetic (CSEM) surveys.

In order to test the above-mentioned hypothesis, we measured the anisotropic physical properties of four mafic and four ultramafic samples drilled in the central dome and the southern wall of the Atlantis Massif at 30°N along the Mid-Atlantic Ridge (IODP Expedition 304-305; Blackman et al., 2006, and 357; Früh-Green et al., 2017, 2018). Ultrasonic *P* and *S* wave velocities, the anisotropic electrical resistivity, and the permeability of the rock samples were measured simultaneously, under differential pressures of up to 45 MPa. The physical properties of four ultramafic samples used in this study were first described by Falcon-Suarez et al. (2017), along with the methodology and the detailed description of the experimental rig used for measurements. Here we compare the physical properties of these ultramafic samples with those of mafic samples from the same region and with mafic and ultramafic samples from other regions. We also compare our homogenous anisotropic electrical resistivity inversion results with the anisotropy observed in thin sections from the same samples. Our simultaneous measurements of anisotropic electrical resistivity and permeability also allow us to explore the use of resistivity as a proxy for permeability. The permeability of the rocks controls the fluid circulation within the rock matrix and therefore affects the rheology via alteration and heat transfer.

2. Tectonic Setting of Atlantis Massif

The Atlantis Massif is an OCC located at 30°N, 15 km west from the axis of the slow-spreading (full-spreading rate ~23.6 mm/a; Grimes et al., 2008; Zervas et al., 1995) Mid-Atlantic Ridge (Figure 1). It is a 20 by 15 km, dome-shaped massif corresponding to the footwall of a large-offset normal fault interpreted as a detachment fault. The massif is composed of a central dome and a southern wall and is bordered to the east by a basaltic ridge that is interpreted as a part of the hanging wall.

The southern wall of Atlantis Massif exposes a cross section throughout the OCC, which is interpreted as being composed of serpentinized peridotite intruded by gabbro lenses and capped by a 100-m-thick detachment fault shear zone (Karson et al., 2006; Schroeder & John, 2004). The highest point of the southern wall (~800-m water depth) hosts the Lost City Hydrothermal Field (LCHF), an off-axis serpentinite-hosted hydrothermal system (Früh-Green et al., 2003; Kelley et al., 2001, 2005).

In 2004–2005, IODP Expeditions 304-305 cored and logged a ~1.4-km hole (U1309D; Figure 1) at the central dome of the Atlantis Massif (Blackman et al., 2006, 2011). In contrast to predrilling interpretations, Expedition 304-305 recovered 91% moderately deformed gabbroic rocks. Prior to the expedition, the role of serpentinization in strain localization during periods of reduced magma supply was known in OCC formation (Escartín et al., 2003; Tucholke & Lin, 1994). The discovery of the gabbroic pluton below the central dome allowed the development of a new hypothesis for the mechanism of formation of OCCs composed of a gabbroic body surrounded by serpentinized peridotite host (e.g., Atlantis Massif, 15°20′N; Ildefonse et al., 2007). The presence of the gabbroic body is explained by an episodically enhanced magma supply toward the segment end. With cessation of the enhanced magma supply, the resulting magmatic body rises by buoyancy and cools slowly. Magmatic fluids and/or seawater-derived hydrothermal fluids initiate the serpentinization around the gabbroic pluton. Steeply dipping faults form following the weakened zone surrounding the pluton, which in turn allows strain localization along the detachment fault and exposure of the serpentinized

Table 1
Summary of the Samples Used in the Present Study

Sample	Leg	Site hole	Core section	Interval(cm)	Latitude	Longitude	Top depth (m bsf)	Bulk density (kg/m^3)	Grain density (kg/m^3)	Porosity (%)
S1	357	M0068-B	1R-1-W	12–18	30.125°N	42.096°W	0.12	2,790	2,830	2.58
S2	357	M0076-B	8R-1-W	120–128	30.127°N	42.118°W	12.356	2,370	2,530	10.41
S4	357	M0076-B	7R-1-W	77–83	30.127°N	42.118° W	10.004	2,480	2,600	7.64
S5	357	M0069-A	10R-3-W	2–9	30.132°N	42.120°	16.49	2,410	2,610	12.78
S7	304	U1309-D	47R-3-W	32–39	30.168°N	42.119°W	250.42	2,840	2,860	0.89
S8	304	U1309-B	9R-1-W	54–60	30.169°N	42.119°W	47.5	2,860	2,910	2.90
S9	304	U1309-D	11R-1-W	110–116	30.168°N	42.119°W	64.9	2,860	2,870	0.97
S10	304	U1309-D	17R-3-W	25–31	30.168°N	42.119°W	101.26	2,840	2,890	2.59

Note. S1 to S5 and S7 to S10 are ultramafic and mafic samples, respectively. The sample interval gives the position of the sample within the core section, and the top depth is the in situ depth of the sample.

peridotite and gabbroic pluton to the seafloor (Ildefonse et al., 2007). The seafloor bathymetry of the Atlantis Massif with greater uplift of the southern wall than of the central dome to the northwest is explained by a second episode of enhanced magmatism, which affected only the northern part of the massif. This second magmatic episode ended the detachment activity at the central dome, while the southern wall which was cooler continued to uplift for longer (Blackman et al., 2011).

In October to December 2015, IODP Expedition 357 cored an E-W transect across the southern wall of the Atlantis Massif. The objectives of this expedition were to examine the role of serpentinization in deriving hydrothermal systems, sustaining microbiological activity and sequestrating carbon; to characterize the tectonic processes leading to lithospheric heterogeneities and detachment faulting; and to assess the changes in abiotic and biotic processes with rock type and exposure to the seafloor (Früh-Green et al., 2016). A total of nine sites was drilled across the massif (Figure 1). Two sites sampled the eastern end of the southern wall. Three sites were drilled at the central part of the southern wall, where the LCHF is located. Two sites sampled the western end of wall, and two aborted sites were drilled north of LCHF.

3. Materials and Methods

3.1. Sample Selection and Preparation

Four mafic and four ultramafic samples from the Atlantis Massif were used for this study (Table 1 and Figure 2). The mafic core samples were acquired at the central dome of the Atlantis Massif, during IODP Expedition 304-305 from the holes U1309-B and U1309-D (Blackman et al., 2006, 2011) at depths ranging between 47.5 and 250.42 m. The ultramafic samples were acquired from the southern wall of the Atlantis Massif, during IODP Expedition 357 (Früh-Green et al., 2016). We received six ultramafic core samples from Expedition 357, but two of them could not been used for this study. To conserve the same naming as in Falcon-Suarez et al. (2017), we named the ultramafic samples from 1 to 6 and mafic samples from 7 to 10. Three ultramafic samples were extracted from the central sites (M0069-A and M0076-B) that sampled the southern wall near the LCHF and one from the eastern site (M0068-B), corresponding to the younger part of the exposed detachment footwall (Figure 1; Früh-Green et al., 2017). The in situ depths of ultramafic samples range between 0.12 and 16.49 m bsf (Table 1).

All ultramafic samples analyzed in this study come from the detachment shear zone that is documented to be 100 m thick at the southern wall (Karson et al., 2006; Schroeder & John, 2004). On the contrary, the detachment shear zone is thin (<20 m) at the Central Dome (Harding et al., 2016), and the mafic samples come mostly from the deeper and broader deformation zone, well below the detachment shear zone. The experimental rig that we used for the physical properties measurements requires cylindrical samples of 5-cm diameter and ~2-cm height. Hence, sample selection was limited by the availability of intact (not broken) core of sizes large enough to allow the extraction of samples required by the experimental rig. Therefore, the most relevant, small suit of mafic samples from the IODP Expedition 357 or the ultramafic samples from Expeditions 304-305 could not been used for this study.

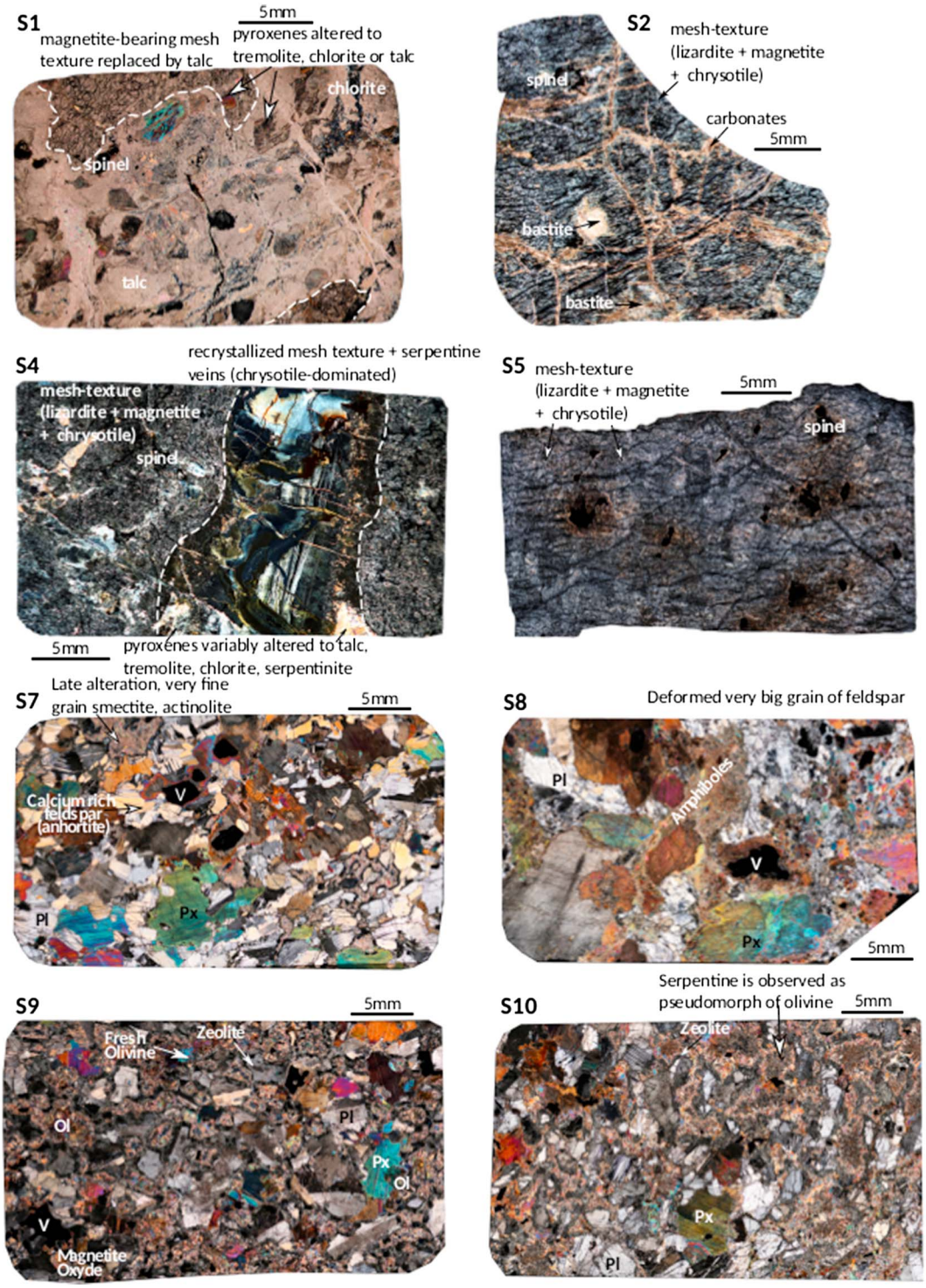

Figure 2. High-resolution thin section images under cross-polarized light. Top four are ultramafic samples from the Integrated Ocean Discovery Program Expedition 357 (S1 to S5) and bottom four are the mafic samples from the Integrated Ocean Discovery Program Expedition 304-305 (S7 to S10). Ol, Px, and Pl stand for olivine, pyroxene, and plagioclase, respectively.

Cores were bisected along their vertical axes, and working halves of the cores were subsampled as 6-cm half cores in the IODP core repository. From the half cores, we extracted 5-cm diameter, ~1.7-cm height samples (hereafter denoted as minicores), cored perpendicularly to the elongation axes of the original core. Then the

Table 2
Modal Composition From Analysis of High-Resolution Thin Section Images

Ultramafic samples	Ol	Px	Sp	Secondary minerals				Alteration
				Serp	Chl + Tr + Act	Tc	Carb	
S1	80°	20°	<1	0	10	90		100
S2	90°	10°	<1	90			10	100
S4	80°	14°	1	85	1			100
S5	95°		5	95				100
Mafic samples	Ol	Px	Pg	Secondary minerals				Alteration
S7	<1	32	56	Hbl	Chl + Tr + Act		Mag + Ilm	12
S8	0	33	44	Hbl	Chl + Tr + Act			23
S9	4	10	32		Chl + Tr + Act	Zeo	Clay	32
S10	0	10	38		Chl + Tr + Act	Zeo		38

Note. Ol = olivine; Px = pyroxene; Sp = spinel; Pg = plagioclase; Serp = serpentine; Chl = chlorite; Tr = tremolite; Act = actinolite; Tc = talc; C = carbonate; Hbl = hornblende; Mag = magnetite; Ilm = ilmenite; Zeo = zeolite. The ultramafic samples are all altered 100%, and the original mineralogy has been interpreted from percentage of various alteration products. Degree symbol against the primary mineralogy of ultramafic samples indicates that these values have been deduced based on alteration products.

minicores were saturated in degassed 35 g/L NaCl-brine (resistivity ~0.19 Ω m). Further details of the sample preparation procedure can be found in Falcon-Suarez et al. (2017).

3.2. Thin Sections

For samples S1, S2, S7, S8, S9, and S10, one vertical and one horizontal thin sections were prepared from the remaining trimmings after minicoring. Due to moratorium period obligations, we could not cut the minicore frames of ultramafic samples S4 and S5. For these samples, we used horizontal thin sections cut immediately adjacent to our 6-cm half cores at the IODP core repository. Vertical thin sections were cut from the flat core splitting surfaces (up-core direction was indicated for each thin section). Horizontal thin sections were cut from the top or bottom flat surface of the half-core samples.

Thin sections were analyzed under a standard petrographic microscope, and photos of whole thin sections were used to estimate mineral modal proportions within the samples. For mafic samples, we attributed a color to each mineral and colored each corresponding mineral grain accordingly. We calculated the proportion of each mineral based on the area covered by each color, using ImageJ software (Rasband, 1997). Since the ultramafic samples were highly serpentinized, individual grains were indistinguishable, and the color method could not be applied. Instead, textures of ultramafic samples were analyzed under the microscope, and zones with different types of serpentinite and other alteration products (e.g., talc/smectite) were identified, and their percentages were estimated visually. Table 2 summarizes the mineral contents of our samples.

Fractures, veins, and grain boundaries were detected by the Sobel edge detection algorithm of the GNU Image Manipulation Program software (Kylander & Kylander, 1999). Whenever it was possible, the detection was carried out in both horizontal and vertical thin sections (all samples but S4 and S5, for which we only had horizontal thin sections). Colored, high-resolution thin section images were separated in Lab color space (L component describes the lightness and a and b components the colors from green to red and from blue to yellow, respectively; Lakio et al., 2010); the lightness component was used for edge detection. A Gaussian blur filter was applied before edge detection to detect only major edges and to avoid detecting mineral internal color changes. The orientation and length of major and minor axes of continuous edges were plotted as rose diagrams of grain and vein orientations (Figure 3). In order to avoid considering the borders of the thin section as fractures, veins, or grain boundaries, rose diagrams were calculated on circle-shape subareas of the same diameter cut from each thin section. Hence, rose diagrams are not representative of the whole sample but of a specific location on the thin section.

3.3. Experimental Procedure and Measurements

The bulk density (ρ_b) of minicores was determined by dividing the weight of brine saturated samples by their bulk volume, calculated from the height and radius of samples (Table 1 and Figure 4). Pore volumes within samples were estimated using the difference between brine saturated and dry weights and the density of

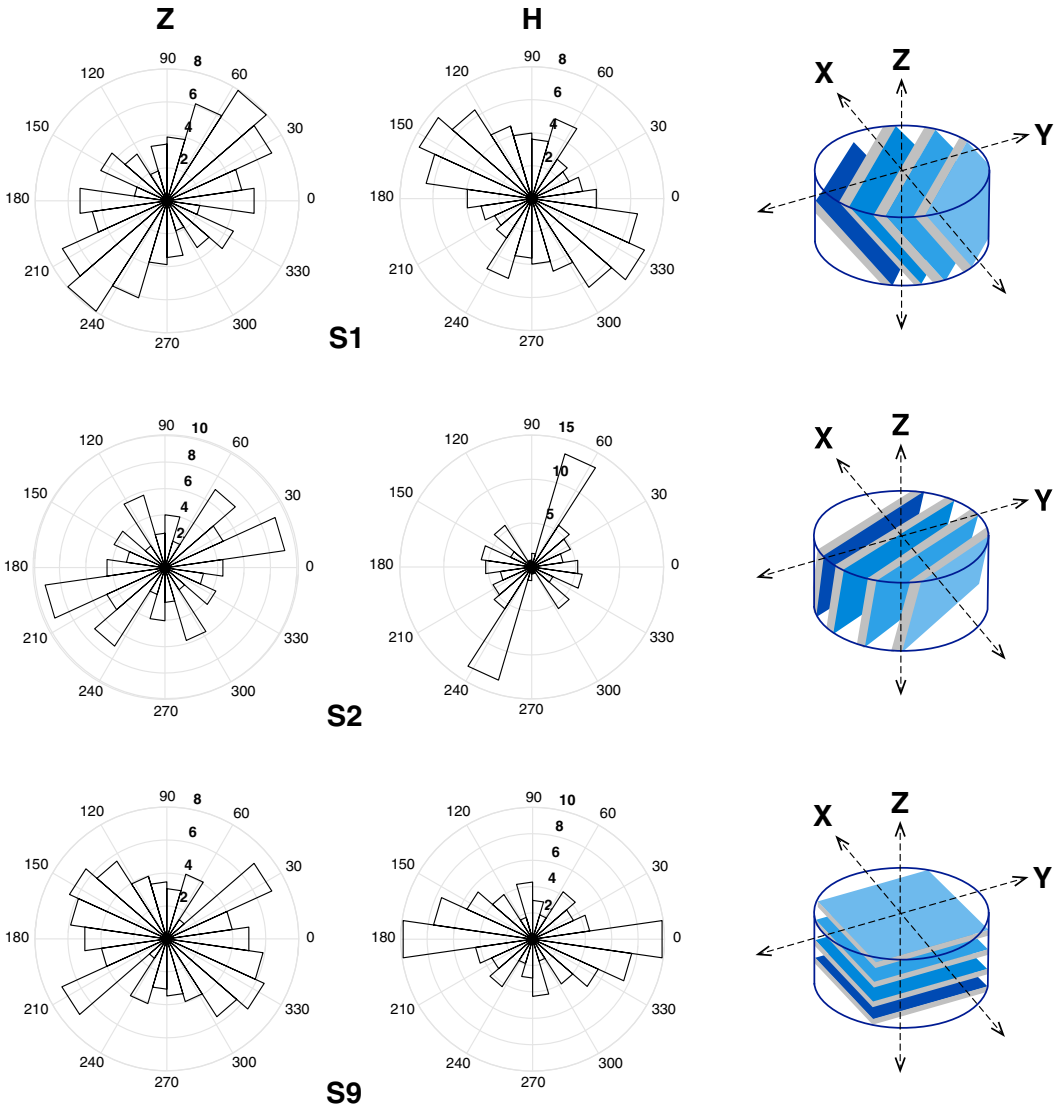

Figure 3. Rose diagrams of fracture, vein, or mineral boundary orientations obtained with image processing of vertical and horizontal thin sections. (top) S1, 357 68B 1R1 12–18 cm; (middle) S2, 357 76B 8R1 120–128 cm; and (bottom) S9, 304 U1309–D 11R1 110–116 cm. The left and middle columns show vertical and horizontal thin sections in core coordinate frame, respectively. In the minicore coordinate frame, the vertical thin sections correspond to the top view, and the horizontal ones correspond to vertical cross sections. The right column shows the schematic representation of the foliation (or lineation) within minicores.

the brine (1,025 kg/m^3 for a salinity of 35 g/L at constant temperature of 19 °C). Porosity (ϕ) or percent pore volume was then calculated using the ratio of pore volume to the bulk volume. The grain density (ρ_s) was estimated by dividing the dry mass by the grain volume, which is calculated by subtracting the pore volume from the bulk volume.

The experiment was carried out using the high-pressure, room-temperature multifluid experimental rig at the National Oceanography Centre, Southampton (Falcon-Suarez et al., 2016). The rig allows simultaneous measurements of *P* and *S* wave velocities and their attenuations, resistivity, and permeability of 5-cm diameter and up to 2.5-cm length rock samples, under up to 60 MPa of pressure. Permeability (k), *P* and *S* wave velocities (V_p and V_s), and resistivity were all measured for a set of differential pressures ($P_{diff} = P_c - P_p$; P_c: confining pressure, P_p: pore pressure), by keeping constant the pore pressure at 5 MPa while varying the confining pressure in a hydrostatic mode (i.e., $P_c = \sigma_1 = \sigma_2 = \sigma_3$) from 10 to 50 MPa, 10-MPa stepwise, under drained conditions. To account for potential hysteresis effects, two unloading steps at 30 and 10 MPa completed the differential stress path (Falcon-Suarez et al., 2017).

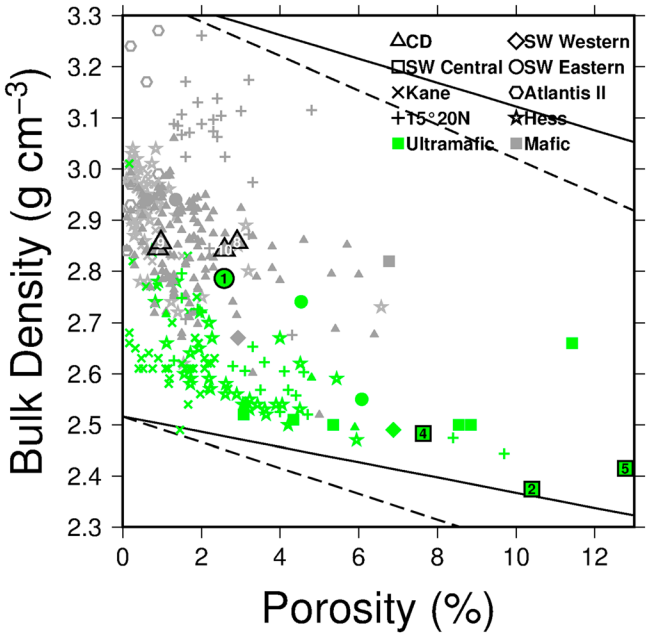

Figure 4. Porosity versus bulk density at room *T*/*P* of mafic (gray) and ultramafic (green) samples acquired from Atlantis Massif and worldwide. (CD) Integrated Ocean Discovery Program Expedition 304-305, Holes U1309-B and U1309-D; (Blackman et al., 2006). (SW) Integrated Ocean Discovery Program Expedition 357, (western sites) M0071 and M0073; (central sites) M0069, M0072, and M0076; and (eastern sites) M0068 and M0075 (Früh-Green et al., 2017). (Kane) Kane transform fault, ODP Leg 153, Holes 920-D and 923-A (Miller & Christensen, 1997). (Atlantis II) Atlantis II fracture zone, ODP Leg 118, Hole 735-B (Iturrino et al., 1991) and 15° 20′N: 15° 20′N fracture zone, ODP Leg 209; Holes 1274-A and 1275-B (Kelemen et al., 2007). Continuous and dashed black lines show the theoretical density decrease with increasing porosity for pristine peridotite (top) and serpentinite (bottom) for dry and water saturated conditions respectively. ODP = Ocean Discovery Program; CD = Atlantis Massif central dome; SW = Atlantis Massif southern wall.

P and *S* wave velocities were measured using the pulse-echo technique with accuracies of ±0.3% (Best et al., 2007; McCann & Sothcott, 1992). Resistivity (ρ) was measured with an array of 16 electrodes distributed in two rings of eight around the core (North et al., 2013; North & Best, 2014). The electrodes were connected to an electrical resistivity tomography data acquisition system which acquires 208 individual tetrapolar measurements using various permutations of current injection, and potential difference sensing electrode pairs were acquired during each acquisition run. These data were then inverted using a nonlinear finite element inversion methods to obtain the homogeneous intrinsic anisotropic resistivity of the sample. Sensitivity tests for the anisotropic inversion have been carried out with the methodology described in North and Best (2014). Permeability was measured using steady state flow method based on Darcy's law, whenever the permeability was high enough to allow a steady flow-through condition. For low permeability measurements, we used the pore pressure transmission method instead, based on transient states of the pore pressure. Further details of the permeability methods used in this work are given by Falcon-Suarez et al. (2017).

4. Results

4.1. Thin Section Descriptions

Here we summarize the petrography of the ultramafic samples S1 to S5 presented by Falcon-Suarez et al. (2017) and similarly describe the four additional mafic samples used in this study.

All samples are altered, to different degrees, by aqueous fluids, most likely seawater-derived hydrothermal fluids. A general description of the peridotite alteration in holes from IODP Expedition 357 is available in Rouméjon et al. (2018).

S1 is a metasomatized serpentinized peridotite (Figure 2). The sample is fully altered, and olivine is replaced by a magnetite-bearing lizardite with mesh texture. Pyroxene is partially altered to tremolite, chlorite, or talc. A pervasive silica metasomatism led to an almost complete replacement of the serpentine by talc yet preserving the magnetite content of the mesh texture.

S2 is a serpentinized harzburgite with low pyroxene abundance, close to dunitic composition (Figure 2). Primary olivine is replaced by a lizardite-dominated and magnetite-bearing mesh texture, and pyroxenes are altered to bastites. The mesh texture is crosscut by thin serpentine veins and a prominent late carbonate vein network.

S4 is a porpyroclastic serpentinized harzburgite with a lizardite-dominated mesh texture. It contains domains where the mesh texture is fully replaced by recrystallized serpentine (chrysotile and antigorite; Figure 2). Magnetite is abundant and is mainly restricted to the mesh textures and to the vein walls. Pyroxenes are mostly altered to serpentine, tremolite, chlorite, and talc.

S5 is a fully serpentinized dunite, dominated by a magnetite-bearing mesh texture (lizardite ± chrysotile). Spinel is equally distributed over the sample (Figure 2), and the magnetite is mainly present along fractures.

S7 is a coarse-grained olivine gabbro with large (>2 mm) pyroxene and feldspar (anorthite) crystals (Figure 2). On both horizontal and vertical thin sections, only few and smaller olivine grains were observed. This sample is the freshest of all of the samples, with only very minor replacement of pyroxene by amphibole and chlorite and generally fresh plagioclase. Olivine crystals are mostly fresh in their cores but show abundant fractures and alteration rims or a partial replacement by chlorite, tremolite, and talc.

S8 is a coarse-grained gabbro with grain sizes >5 mm (Figure 2). Due to deformation, the twinning of feldspar crystals is not always observed, and partially, some feldspar grains are recrystallized into smaller subgrains. No particular alignment related to shearing is observed. Pyroxene is partially altered to a mix of tremolite, actinolite, and chlorite. No fresh olivine is observed.

S9 is a medium-grained olivine gabbro (Figure 2). Olivine is partially fresh, but most grains show a pronounced alteration rim of tremolite, chlorite, and actinolite, similar to pyroxene alteration assemblages. Pyroxenes show some replacement by amphiboles but are mostly fresh. Most plagioclase are altered to zeolite, with zeolites surrounding still fresh plagioclase cores. The presence of zeolite suggests that this sample experienced low temperature alteration with low carbon dioxide aqueous fluids, possibly derived from seawater or hydrothermal fluid infiltration.

S10 is a highly altered coarse-grained gabbro (Figure 2). Whereas plagioclase shows abundant fractures and is rimmed by zeolites, pyroxenes are variably altered to actinolite, tremolite, and minor amounts of chlorite. The alteration products suggest an alteration with a hydrothermal fluid, possibly seawater derived. No olivine has been observed in the associated thin section.

The rose diagrams of grain and vein orientations (Figure 3) show some anisotropy for all samples except the S5 (not shown), which is a serpentinized dunite with clear mesh texture (Figure 2). S1 and S2 show anisotropy on both vertical and horizontal thin sections, whereas no clear anisotropy direction is visible on the vertical thin section of S9. S1 shows an anisotropy orientation of ~45° to the horizontal, whereas the anisotropy within S2 is closer to horizontal, at ~20°. S9 does not show clear anisotropy on the vertical thin section. On the horizontal thin sections, S1, S2, and S9 exhibit vein and fracture orientations of 150°, 70°, and 5°, respectively (Figure 3).

Cores acquired during IODP Expedition 357 have not been oriented. Morris et al. (2009) have reoriented 34 core pieces distributed within the upper 100 to 400 m of the Hole U1309-D by matching the individual core structures to their representation on oriented Formation MicroScanner borehole images. They have calculated a mean in situ magnetization direction (declination = 226.1°, inclination = −38.1°, α_{95} = 4.4°, N = 62) which allows the reorientation of core pieces from this hole by rotating the piece average magnetization to the mean declination (Pressling et al., 2012). We did not reorient out mafic samples using the mean declination because two of them were from the upper 100 m of the Hole U1309-D and a third one was from the Hole U1309-B. Only the uphole direction was indicated on all vertical thin sections. Hence, the data do not allow us to infer the azimuthal orientation of anisotropy. Moreover, the edge detection method has limitations. The analysis is carried out on circle shape subarea; hence, only a subset of veins and grain boundaries are considered. S1 and S2 show anisotropy in both vertical and horizontal sections, which suggests a foliated structure. S9 exhibits anisotropy only in the horizontal thin sections and not on the vertical one, but it may still contain a preferred orientation in the vertical direction perpendicular to the core splitting surface.

4.2. Bulk Density, Porosity, and Grain Density

Bulk densities of ultramafic samples (2,370 to 2,790 kg/m^3) are lower and do not overlap with those of mafic samples (2,840 to 2,860 kg/m^3), which show smaller variation (Table 1 and Figure 4). The porosities of ultramafic and mafic samples are 2.51–12.47% and 0.89–2.90%, respectively (Table 1 and Figure 4). Only the talc-rich sample S1 shows a porosity similar to the mafic samples and a density higher than other serpentinized harzburgite and dunite samples. The grain densities of mafic and ultramafic samples are 2,860–2,910 and 2,530–2,830 kg/m^3, respectively, suggesting that the ultramafic samples do not only exhibit low density because of their high porosity but also because they are made of lower-density grains than the mafic samples.

4.3. Seismic Velocities

At the minimum differential pressure (5 MPa), *P* and *S* wave velocities of our mafic samples varied between 5.92 and 6.70 km/s and 3.36 and 3.62 km/s, respectively (Figure 5). Ultramafic samples ranged between 3.28 and 4.87 km/s and 1.67 and 2.34 km/s, due to their higher degree of alteration and porosity. As expected, the velocities correlate with density (Birch, 1961).

For both mafic and ultramafic rocks, the primary source of velocity increase below 200 MPa is the closing of microcracks and pores (Hyndman & Drury, 1976; Miller & Christensen, 1997). Ultramafic samples exhibit more rapid velocity increase with increasing pressure, attributed to a higher pore volume compressibility effect (i.e.,

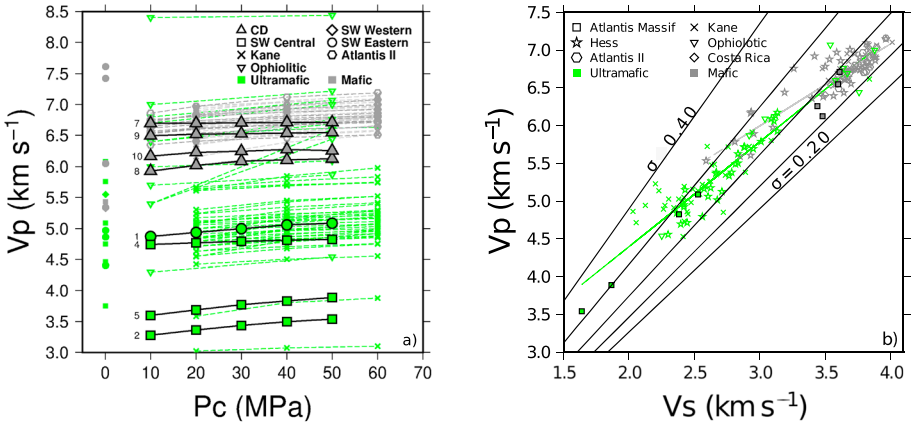

Figure 5. (a) Confining pressure versus *P* wave velocity. Green symbols represent ultramafic samples and gray ones the mafic samples. Symbol shape represent the location of acquisition. The sample number is shown next to each sample measured in this study. (b) *P* wave velocity versus *S* wave velocity of the mafic and ultramafic samples under the confining pressure of 50 MPa. (squares) Atlantis Massif (central dome; Integrated Ocean Discovery Program Expedition 304-305: Holes U1039-B and U1039-D; Blackman et al., 2006; and southern wall; Integrated Ocean Discovery Program Expedition 357; Holes M0069A, M0076B, and M0068B; Früh-Green et al., 2017), (crosses) Kane transform fault (ODP Leg 153; Holes 920-D and 923-A; Miller & Christensen, 1997), (stars) Hess Deep (ODP Leg 147, Sites 894 and 895; Iturrino et al., 1996), (diamonds) Costa-Rica rift (ODP Leg 111; Hole 504-B; Christensen et al., 1989), (triangles) Atlantis II fracture zone (ODP Leg 118; Hole 735-B; Iturrino et al., 1991), and (inverted triangles) ophiolitic partially serpentinized peridotites (Christensen, 1966). Black lines show Poisson's ratios between 0.40 and 0.20 with an interval of 0.5. Gray and green lines show the least squares curves for V_p/V_s of ultramafic and mafic samples, respectively. Mafic and ultramafic samples measured in this study are the squares surrounded by black lines. ODP = Ocean Discovery Program.

higher porosity; Figure 5a). The *P* wave velocities of the serpentinized dunite S5 and serpentinized harzburgite S2 with minor pyroxene content are both lower than those of the other two ultramafic samples, with a greater increase (more than 7%) at a differential pressure of 45 MPa, likely related to greater porosity reduction of these samples. Among mafic samples, S8 that is affected by brittle deformation shows the highest *P* wave velocity increase with increasing pressure (Figure 5a).

Poisson's ratios of mafic samples vary between 0.25 and 0.3 and are within the typical range for oceanic layer 3 (Christensen et al., 1975). In our ultramafic samples, this value increases up to more than 0.35 (Figure 5b).

4.4. Electrical Resistivity

At the minimum differential pressure (5 MPa), the resistivity of mafic samples varies between 60 and 221 Ω m, while the ultramafics range between 8 and 44 Ω m (Figure 6). In contrast to wave velocities, mafic samples show higher resistivity increases with increasing differential pressure than ultramafic ones. This effect can be attributed to a more effective closure of connected pore space of mafic samples below 45 MPa, particularly significant (higher resistivity) for the less altered mafic samples S7 and S8 (Table 2 and Figures 2 and 6). In contrast, S5 and S2, with compositions close to dunite, show similar minimum resistivity and less resistivity increase with increasing pressure.

For S2, the original fluid path network is substantially modified at high differential pressure (above 35 MPa) and remains approximately constant onward, despite the unloading (Figure 6).

The homogeneous anisotropic resistivity inversion results (under P_{diff} = 45 MPa) show one high and two similar and lower resistivity axes, for all samples (Figure 7). Serpentinized dunite sample S5 exhibits 33% resistivity anisotropy, whereas all other ultramafic samples range between 88% and 99%. Olivine-bearing mafic samples S7 and S9 showed higher anisotropies (131% to 190% at 45 MPa) than other samples (Table 2 and Figure 7).

4.5. Permeability

The permeability of ultramafic samples varied between 3.2×10^{-15} and 1.1×10^{-18} m^2 (Figure 8) at the minimum differential pressure of 5 MPa. Mafic samples exhibit lower permeability. We were only able to measure the permeability of two highest permeability mafic samples; the permeability of the remaining two samples

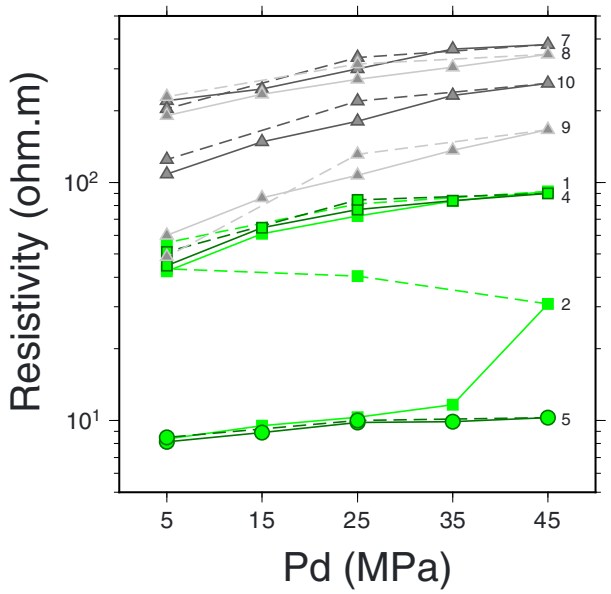

Figure 6. Resistivity as a function of differential pressure. Gray and green symbols represent mafic and ultramafic samples, respectively. Lines are used for visual identification of pressure paths of the samples. Dashed lines show unloading pressure paths. Triangles, squares, and circle represent central dome and southern wall central and eastern samples, respectively. Sample names are indicated next to the sample symbols.

was too low to be measured with our experimental rig. At 5 MPa, the permeability of mafic samples S9 and S10 varied between 10^{-19} and 1.9×10^{-21} m^2. The permeabilities of ultramafic samples are lower than those of gabbro samples at all pressure conditions. Regardless the rock type, our higher permeability samples show higher decrease in permeability with increasing pressure (Figure 8). We observe up to 5 orders of magnitude of difference between our ultramafic and mafic samples at 45 MPa of differential pressure.

5. Discussion

5.1. Bulk Density and Porosity

The bulk density of Atlantis Massif central dome mafic samples measured in this study and their porosity (Table 1) are in the same range as those measured during IODP Expedition 304-305 at Site U1309 (2,500–3,060 kg/m^3 and <5.7%). The bulk density and porosity of southern wall serpentinized peridotites measured during IODP Expedition 357 range between 2.48 and 2,740 kg/m^3 and 3.07% and 11.43%, respectively (Früh-Green et al., 2017). S2 and S5 show lower density than those measured during IODP Expedition 357, and S5 shows higher porosity. S5 is a serpentinized dunite, and S2 is a serpentinized harzburgite with poor pyroxene content, close to dunite. Both samples show serpentinization-related density decrease, and they contain high fractions of mesh texture which increases the porosity. S2 contains carbonates crystalized as a later phase, using the preexisting porosity which may explain the lower porosity of this sample compared to S5. Serpentinized dunites with well-developed mesh texture having higher porosity and lower density than serpentinized harzburgite have been reported also for samples from the Hess Deep (Mével & Stamoudi, 1996) and from 15°20′ N fracture zone (Kelemen et al., 2007).

In sample S4, focused fluid flow led the recrystallization of the mesh texture (lizardite to crysotile), and in sample S1, talc development is due to the interaction between the serpentinite and silica-rich fluids (derived from interactions with mafic rocks; Boschi et al., 2006). Recrystallization-related increases in density affect both samples but is observed in higher proportions in S1. The samples that bear recrystallized textures are interpreted to have been the most permeable domains in the peridotite that channel hydrothermal fluids. Similarly, talc metasomatism is a marker of silica-rich fluids and of preferential fluid pathways in fault zones (Boschi et al., 2006). The lower porosity of samples S1 and S4, affected by recrystallization, suggests that channeling fluids in specific domains led to the reactions that ultimately reduced the porosity (Figure 4) and the permeability (Figure 8).

Regardless the rock type, samples from the southern wall central sites measured during this study and during the onshore science party show higher porosities and lower densities than other southern wall and central dome samples. Expedition 357 was designed as a E-W transect with western sites sampling the exposed and inactive part of the footwall near the breakaway originated from shallow depths and the eastern sites sampling the deeper part of the footwall originated from depths of several kilometers (Figure 1). Along the transect, the age of the lithosphere increases westward by 1 Myr. Therefore, one would expect to observe higher densities and lower porosities westward, with the increasing age of the lithosphere. Several phases of alteration as a consequence of the LCHF may have increased the porosity and decreased the bulk density of some of the central site samples, although the central site samples measured in this study do not show Lost City-related alteration.

Mafic and ultramafic samples from the Kane transform fault show lower porosities and higher densities than the Atlantis Massif samples (Figure 4). A lower degree of alteration was reported for both mafic and ultramafic samples from Kane transform fault (Cannat et al., 1995). The locations of Sites 920 and 923 were approximately 10 km west of the Mid-Atlantic Ridge, and this off-axis location might explain their lower porosities. Heterogeneous access to hydrothermal fluids controlled by fracturing and by the locations of gabbroic

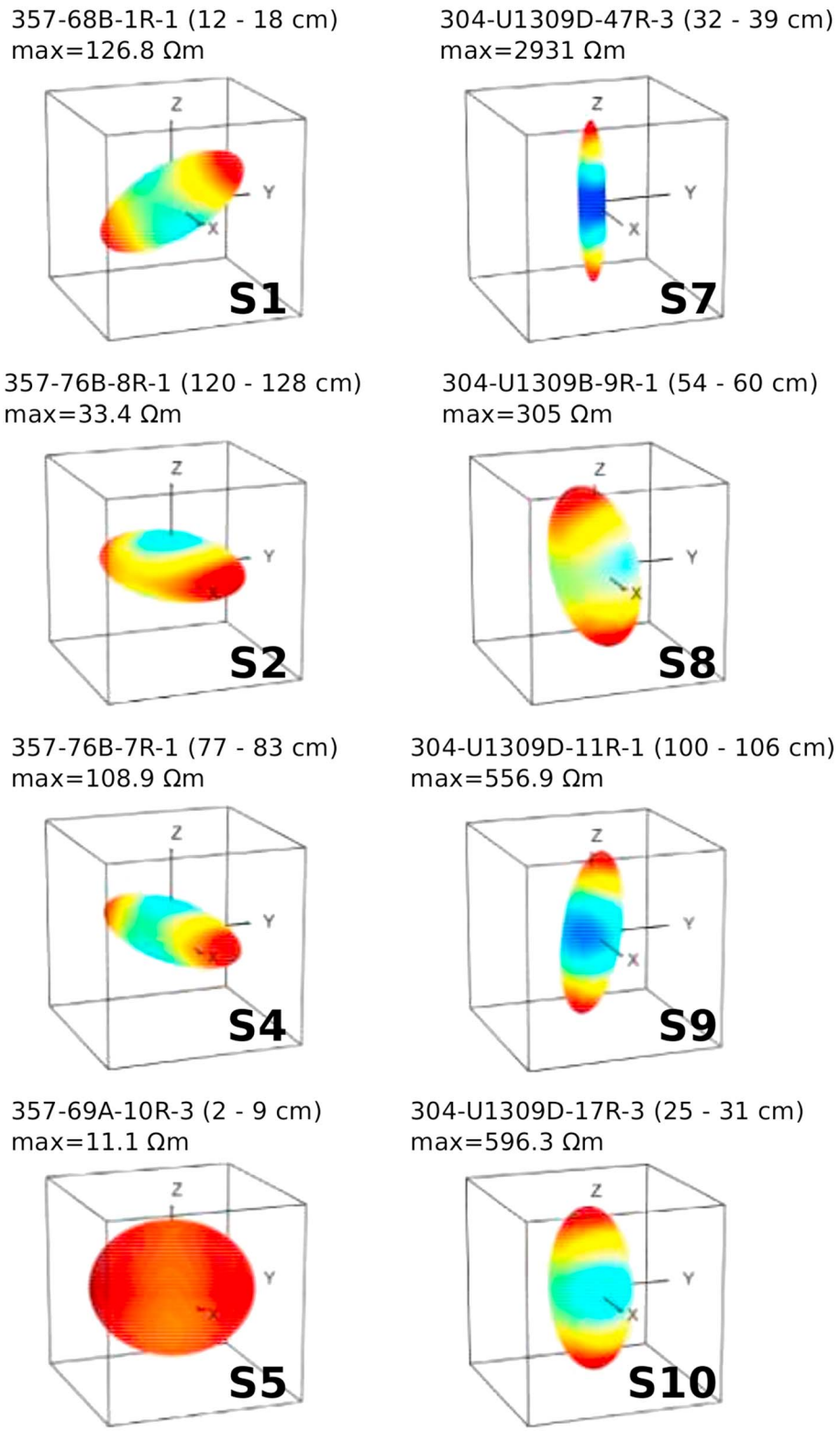

Figure 7. Results of anisotropic resistivity inversion (P_{diff} = 45 MPa) in minicore coordinate frame, normalized by the maximum resistivity value of each sample. Note that here the maximum electrical resistivity is the result of anisotropic resistivity inversion, and it is not equal to the mean electrical resistivity shown in Figure 6. Red shows low resistivity, and blue is high resistivity. The left column show the results for ultramafic samples and right one for mafic samples.

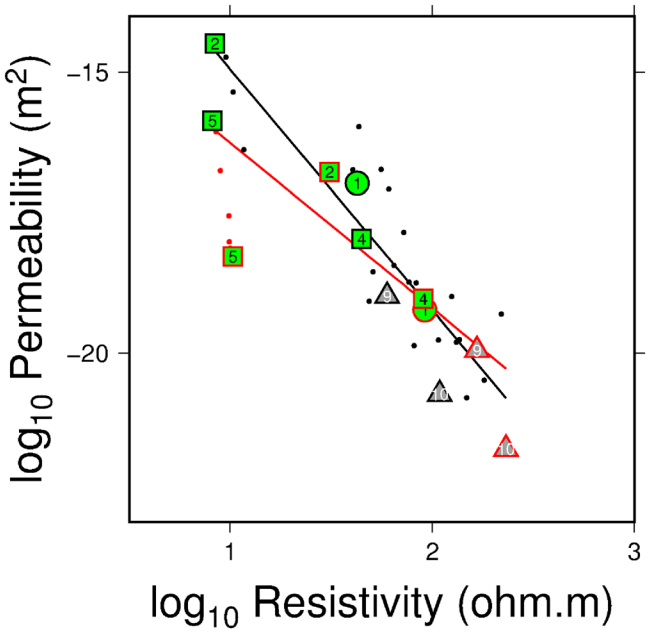

Figure 8. Correlation between permeability and resistivity. Gray and green symbols represent mafic and ultramafic samples, respectively. Symbols surrounded by black represent the measurements under 5 MPa of differential pressure, whereas those surrounded by red are under 45 MPa. The black points are data points at other differential pressures. The black line is the logarithmic regression curve for serpentinized harzburgite (1, 2, and 4) and gabbroic (9 and 10) samples for which the permeability is related to the resistivity with a power law. The dunite sample S5 does not follow this law. Red line shows the regression curve when we consider S5. Red points are the data points of S5 at other differential pressures.

intrusions that act as impermeable cores and help to preserve relatively fresh peridotite at the contact (Blackman et al., 2006; Rouméjon et al., 2018) may also explain the lower porosities and higher densities observed in Kane transform fault. Mafic samples from Atlantis Bank (Iturrino et al., 1991) and the 15°20′ N (Kelemen et al., 2007) transform fault have also higher densities than those from Atlantis Massif (Blackman et al., 2006; Figure 4). Iron-rich gabbro has been reported at Atlantis Bank Hole 735B and 15°20′ N fault zone Hole 1275B, which could be the reason for higher densities.

5.2. *P* Wave Velocity and Poisson's Ratio

P wave velocities of the samples S2 and S5 under a differential pressure of 45 MPa are 3.54 and 3.89 km/s, respectively. These two samples have higher fractions of mesh texture with bastites that increase the porosity of the samples and decrease their density and velocities. Thin section images (Figure 2) and *P* wave velocities (Figure 5) provide a visual observation of the link between the fraction of mesh texture within the samples and *P* wave velocities, at shallow subsurface conditions. S1, which experienced postserpentinization metasomatic alteration, shows only little remaining mesh texture (Figure 2) and has the highest *P* wave velocity (Figure 5a), while S4 contains recrystallized veins cutting across the mesh texture (Figure 2) and has a higher *P* wave velocity than other serpentinized peridotites samples (Figure 5a).

During onshore science party of IODP Expedition 357, the *P* wave measurements were carried out on smaller cubic samples. Larger samples usually contain larger porosities. The *P* wave velocities of our mafic samples are comparable to those of the few mafic samples measured during the onshore science party. The sample size effect is more visible in higher porosity ultramafic samples than in mafic samples, with higher velocities measured on the smaller samples (Figure 5a).

In our compilation at 50-MPa confining pressure (~2-km depth; Figure 5), *P* wave velocities of mafic and ultramafic samples overlap above 5.5 km/s and *S* wave velocities above 2.6 km/s. Poisson's ratio has been proposed (e.g., Carlson & Miller, 1997) as a possible way of distinguishing between mafic and ultramafic rocks via seismic velocities. Although mafic and ultramafic samples measured in this study have distinct Poisson's ratios, our new compilation shows that, in the shallow subsurface (<50 MPa), the Poisson's ratios of mafic and ultramafic rocks overlap between 0.36 and 0.25.

5.3. Electrical Resistivity

The resistivities of the mafic and ultramafic samples measured in this study do not overlap below 45-MPa differential pressure. Our resistivity values for ultramafic samples are comparable to those measured with multisensor core logger (MSCL) during the IODP Expedition 357 (0.3–57.5 Ω m; Früh-Green et al., 2017). Both mafic and ultramafic samples are in the same range as those measured from near the Kane transform fault (68–1,408 Ω m for mafic samples, 10–103 Ω m for serpenitnized harzburgite, and 3–10 Ω m for serpentinized dunite; Cannat et al., 1995; Evans et al., 2010). Mafic samples from Hess Deep showed a larger resistivity range, and ultramafic samples showed strong inverse correlation with porosity, with dunites exhibiting the lowest resistivity (Gillis et al., 2013). We observe a similar relationship. The lowest resistivity values are observed in samples S5 and S2, with relatively high porosity (>10%) and the highest fraction of a magnetite-bearing mesh texture (Falcon-Suarez et al., 2017).

Two main mechanisms are responsible for electrical conduction in media where grains are highly resistive: electrolytic conduction in connected pore space and surface conduction at the interface between the electrolyte and the mineral (Ildefonse et al., 1997; Ildefonse & Pezard, 2001). Our observations suggest that the pore fluid conduction dominates in both gabbro and serpentinized harzburgite samples with resistivity linearly increasing with increasing differential pressure. All four ultramafic samples contain small amounts

of magnetite within the mesh texture, which affects the bulk resistivity of the rocks. There is no increase in resistivity with increasing differential pressure for the dunite sample S5 and serpentinized harzburgite sample S2 with little pyroxene (Figure 6). This observation suggests that under up to 45 MPa of differential pressure, the porosity within these samples is not yet closed or that surface conduction dominates in these samples with a higher fraction of mesh texture. Magnetite has a resistivity of 4×10^{-5} Ω m, and a connected magnetite network may decrease the resistivity dramatically (Evans et al., 2010). We do not observe a clear correlation between shipboard MSCL slow track magnetic susceptibility measurements (Früh-Green et al., 2017) and our resistivity measurements, but S5 shows the highest magnetic susceptibility measured by MSCL (~10^4 SI. e^{-5}) among our ultramafic samples.

For mafic samples, in addition to porosity, degree of alteration seems to play a role. The lowest porosity sample S7 and the highest porosity sample S8 show higher resistivity than other two more altered samples (Figure 2), suggesting that alteration of mafic samples lowers the resistivity, possibly also via surface conduction (Ildefonse et al., 1997).

5.4. Permeability

The permeability of our mafic samples lies within the range previously determined by laboratory measurements in comparable lithologies at similar pressure conditions (e.g., 2×10^{-22} and 8×10^{-24} m^2 at differential pressures of 10 and 25 MPa, respectively; Trimmer et al., 1980; and 10^{-18} and 10^{-22} m^2 at 0 and 50 MPa, respectively; Katayama et al., 2012). Laboratory permeability measurements are lower than in situ measurements of permeability due to the absence of large cracks on in a sample scale (e.g., 24 to 0.2 10^{-15} m^2 down to 223 m bsf for in situ oceanic gabbros from Atlantis Bank, ODP Leg 118, hole 735B; Becker, 1991).

Our ultramafic samples show higher permeability than previous laboratory measurements of permeability (e.g., Nagasaki, Japan, 10^{-19} to 10^{-22} m^2 at differential pressures of 5 to 50 MPa, respectively; Kawano et al., 2011; 10^{-18} and 10^{-20} m^2 at 0 and 50 MPa, respectively; Katayama et al., 2012). This difference may be related to the sample size since the cited studies used smaller samples (20-mm diameter) than ours. It can also be related to the high porosity of our ultramafic samples related to detachment faulting. The fault damage zone may decrease the permeability by 4 orders of magnitude in the continental crust by fractures around the fault (Manning & Ingebritsen, 1999). A similar effect may occur in slow-spreading oceanic crust. Sheared serpentinite is known to have permeability anisotropy which also could explain the observed mismatch. Up to 50 MPa of confining pressure, the permeability parallel to the foliation of serpentinite is 1 order of magnitude or more higher than that normal to the foliations (Kawano et al., 2011).

Katayama et al. (2012) report that the permeability difference between their gabbro and serpentinite samples becomes more obvious at higher confining pressures, whereas the logarithmic difference of permeability between our gabbro and serpentinite samples decreases with increasing pressure, possibly related also to the very high porosity of our ultramafic samples.

In the absence of a large surface conductivity component, the resistivity of rocks is principally a measure of the connected porosity (Archie, 1942) and thus might be used as a proxy for permeability. We compared our direct measurements of permeability and resistivity (Figure 8). For all samples but the serpentinized dunite sample S5, resistivity relates to the permeability with a power law: $\log_{10} k = -10.666–4.283 * \log_{10} \rho$ (Figure 8; coefficient of correlation [r]: −0.9, possibility of noncorrelation [p]: 3.7420e−13). The mismatch of the dunite sample S5 is probably related to its high content of iron before the alteration, which produced an interconnected magnetite network during serpentinization that is also expressed in the magnetic susceptibility of this sample. Our results show that under shallow subsurface conditions (up to 50 MPa) and in the absence of large surface conductivity, the resistivity can be used to estimate the permeability of gabbroic and serpentinized peridotite samples.

5.5. Anisotropy of the Electrical Resistivity

Regardless of rock type, all samples show transverse isotropy (TI) symmetry, which is typical of a layered microstructure or aligned disk-shaped inclusions (North et al., 2013). The magnitude of this TI anisotropy is defined here as the ratio between the mean of the two lower anisotropy eigenvalues and the higher eigenvalue. The presence of more than one anisotropy causing texture within the sample, for example, parallel planar fracture planes that are not aligned with a preexisting layered rock fabric, can decrease the

magnitude and alter the orientation of the TI anisotropy. In some instances of fabric overprinting, TI-type anisotropy is not present, and all three eigenvalues of the anisotropy tensor are different. Thus, multiple fabric types and orientations will add to and alter the overall resultant anisotropy that is observed.

The anisotropy observed within S5 is significantly lower than that of other samples (33%; Figure 7) possibly due to its higher fraction of mesh texture. However, S2, which also has a high fraction of mesh texture, exhibits a higher degree of anisotropy (99%) suggesting that the anisotropy of the resistivity in this case is influenced by aligned carbonate veins within this sample (Figure 2).

In mafic samples, the percentage of anisotropy seems to be controlled by the fresh olivine content. Higher resistivity anisotropy is observed in mafic samples S7 and S9 (190% and 130%, respectively) containing a little fresh olivine than other mafic samples with no fresh olivine (S8: 72%, S10: 90%; Table 2).

Sample S1 that was originally serpentinized harzburgite but transformed into talc by Si-metamorphism shows a low-resistivity axis that is oblique to the vertical axis of the minicore (Figure 7). All other ultramafic samples show a horizontal low-resistivity axis in the coordinate frame of minicores. On the contrary, in mafic samples, the high-resistivity axis is vertical in the minicore frame (Figure 7). The high-resistivity axis is expected to be perpendicular to the lamination (or foliation). The observed perpendicular directions of high-resistivity axes within mafic and ultramafic samples indicate differences in the orientation of the foliation within lower crustal and upper-mantle rocks likely to have different emplacement histories.

The result of anisotropic homogeneous inversion (Figure 7) is in good agreement with the rose diagrams of grain and vein orientations (Figure 3), which also showed some anisotropy for every sample except the serpentinized dunite sample S5 (not shown). For S1 and S2, anisotropy is observed on both vertical and horizontal thin sections and hence suggests a structure aligned as layers (Figure 3). The high-resistivity axis retrieved by the anisotropic resistivity inversion (Figure 7) is perpendicular to the foliation plane observed on perpendicular thin sections (Figure 3). S9 did not show a particular anisotropy direction on the vertical thin section but showed an orientation of 5° on the horizontal thin section (Figure 3). The result of anisotropic electrical resistivity inversion of S9 shows a vertical high-resistivity and two horizontal low-resistivity axes, suggesting a foliated structure also for this sample. This result is in good agreement with the rose diagrams of this sample and suggests a horizontal foliation plane in the minicore frame (Figure 3).

The minicores were drilled perpendicular to the core slipping surface of working half cores. In the coordinate frame of the core, mafic rocks analyzed in this study show vertically aligned foliation. Our ultramafic samples exhibit a high-resistivity axes that is perpendicular to the high-resistivity axes of the mafic samples. Our sample selection is biased in a specific way since all our ultramafic samples are sampled from the detachment shear zone, whereas our mafic samples are from the deeper and broader deformation zone, well below the detachment shear zone. The movement along the detachment fault might have affected the foliation within our ultramafic samples. However, visual observations of the ultramafic samples recovered from the detachment shear zone do only indicate minor shearing. The resistivity anisotropy observed within our ultramafic samples may result from the preferential orientation of fracturing due to thermal contraction and tectonic stress after the uplift of ultramafic rocks (Rouméjon & Cannat, 2014). Although the observed perpendicular high-resistivity axes in mafic and ultramafic samples is not a direct indication of lithology changes, it suggests that the anisotropy of resistivity can be used as a tool to distinguish between these rocks, via remote CSEM surveying when some regional a priori structural information is available. The electromagnetic profile acquired across the Kane OCC interpreted in combination with the *P* wave velocity distribution of the region has suggested that the sharp transition from conductive to resistive seafloor marks the transition from serpentinized peridotite to either gabbro or pristine mantle rocks (Evans et al., 2010). In the shallow subsurface, the conductive to resistive seafloor transition is mainly controlled by the porosity, which may disappear at depth due to the compaction. A CSEM study run as multiple complete concentric circular tows of different radii, with multiple frequencies to increase the depth resolution, would resolve the anisotropy in depth and allow to distinguish between gabbro and variably serpentinized peridotite with similar porosities via the orientation of the anisotropy (Behrens, 2005).

Vertically aligned foliations of mafic samples observed on both the thin sections and the results of anisotropic resistivity inversion are consistent with buoyancy-driven vertical motion between gabbro and fresh peridotite. Similar vertical magmatic foliation has been observed at structurally high gabbros in Oman that are not highly deformed (MacLeod, Boudier, et al., 1996; MacLeod, Célérier, et al., 1996; Yaouancq & MacLeod,

2000) like the Atlantis Massif mafic samples. Vertical foliation within the gabbroic samples suggests that the gabbroic body has intruded after detachment fault activity, as the foliation is not affected by the footwall rotation of 45° suggested by paleomagnetic data (Morris et al., 2009). Our mafic samples therefore may have been intruded directly within the central dome, which is part of the footwall of the detachment fault 15 km west of the ridge axes, after the footwall rotation, during the second enhanced magmatic episode that stopped the detachment faulting at the central dome of the Atlantis Massif. These rocks may have migrated to their shallow location within the footwall, by a combination of buoyancy-driven vertical motion and flexural uplift of the footwall, due to unloading by slip of the hanging wall along the detachment fault after counterclockwise rotation about a NNW axis of the (footwall) block (Schroeder & John, 2004).

A horizontal foliation within the central southern wall ultramafic samples is in good agreement with direct observations of mylonitic shear zone foliation and samples acquired with the submersible Alvin (Karson et al., 2006). A horizontal foliation (vertical high-resistivity axis) is also observed at a Southwest Indian Ridge detachment shear zone composed of highly deformed gabbro that forms the top of the Atlantis Bank OCC (Ildefonse & Pezard, 2001). Although the shear zone mylonitization temperatures for these two end member OCCs may be very different (Blackman et al., 2011), the orientation of their foliation seems to be similar, and possibly both are affected by elongated pore space aligned parallel to the extension direction.

6. Conclusions

Our mafic and ultramafic samples measured under shallow subsurface conditions (up to 50 MPa) show distinct differences in density, *P* and *S* wave velocities, Poisson's ratio, and resistivity. However, the comparison with mafic and ultramafic samples from other similar regions shows that these physical properties may not allow the differentiation of these rocks remotely.

The result of sample size anisotropic homogeneous resistivity inversion found TI-type anisotropy symmetry (one high and two similar and low-resistivity eigenvalues) in all samples. This type of anisotropy indicates a structure aligned as layers such as a laminated or a foliated structure. In mafic samples, the orientation of the foliation is in a vertical direction, whereas in ultramafic samples, it is horizontal. Retrieved perpendicular high-resistivity axes within mafic and ultramafic rocks are in good agreement with observations on thin sections. Observed and retrieved foliation directions are also in good agreement with the proposed mechanism of OCC formation, with gabbroic rocks intruded during the last enhanced magmatic episode that ceased the activity of the detachment faulting at the central dome of the Atlantis Massif.

Because the cores have not been oriented, we cannot identify the azimuthal direction of the high-resistivity axis within mafic samples with vertical foliation. However, the observed difference in the direction of the high-resistivity axis within mafic and ultramafic samples suggests that controlled source electromagnetic surveys can be a useful tool to distinguish these rocks remotely, if some structural information about the study region is available. In this study we have analyzed four ultramafic and four mafic samples sampled from the detachment shear zone and the deeper and diffuse deformation zone, below the detachment shear zone, respectively. A more comprehensive, systematic, and unbiased sampling and measurements of the anisotropic physical properties of mafic and ultramafic rocks would allow the validation of the approach of using the anisotropic electrical resistivity as a potential indicator of lithology.

Acknowledgments
We acknowledge support from the United Kingdom (UK) Natural Environment Research Council (NERC) and IODP Phase 2 grant NE/N012402/1 and IODP/ECORD for funding the Expeditions 304-305 and 357 and providing samples. The samples used in this study are accessible from IODP Bremen Core Repository (Marum, Germany) upon request. We acknowledge ESO operators as well as the RD2 drill team and the cochief scientists of the Expedition 304-305 and Expedition 357, for enabling the samples to be collected. The experimental apparatus was jointly funded by NERC and the UK Engineering and Physical Sciences Research Council (EPSRC) under a separate program (EP/K035878/1). T. A. M. was supported by a Wolfson Research Merit award. S. R. was supported by Swiss National Science Foundation Grant 200021-163187. The physical properties data set used in this study can be accessed at https://doi.pangaea.de/10.1594/PANGAEA.873535. We thank Donna Blackman for a constructive review.

References

Anderson, D. L. (2007). *New theory of the Earth* (p. 384). New York: Cambridge University Press. https://doi.org/10.1017/CBO9781139167291

Archie, G. E. (1942). The electrical resistivity log as an aid in determining some reservoir characteristics. *Transactions of American Institute of Mining*, *146*(01), 54–62. https://doi.org/10.2118/942054-G

Becker, K. (1991). In-situ bulk permeability of oceanic gabbros in Hole 735B, ODP Leg 118. In *Proceeding of the Ocean Drilling Program*, *Scientific Results*, *118*, 333–347.

Behrens, J. P. (2005). The detection of electrical anisotropy in 35 Ma Pacific lithosphere: Results from a marine controlled-source electromagnetic survey and implications for hydration of the upper mantle, (PhD thesis). University of California, San Diego.

Best, A. I., Sothcott, J., & McCann, C. (2007). A laboratory study of seismic velocity and attenuation anisotropy in near-surface sedimentary rocks. *Geophysical Prospecting*, *55*(5), 609–625. https://doi.org/10.1111/j.1365-2478.2007.00642.x

Bezacier, L., Reynard, B., Bass, J. D., Sanchez-Valle, C., & Van de Moortèle, B. (2010). Elasticity of antigorite, seismic detection of serpentinites, and anisotropy in subduction zones. *Earth and Planetary Science Letters*, *289*(1–2), 198–208. https://doi.org/10.1016/j.epsl.2009.11.009

Birch, F. (1961). The velocity of compressional waves in rocks to 10 kilobars: 2. *Journal of Geophysical Research*, *66*, 2199–2224. https://doi.org/10.1029/JZ066i007p02199

Bird, D. K., Manning, C. E., & Rose, N. M. (1988). Hydrothermal alteration of Tertiary layered gabbros. *East Greenland, American Journal of Science*, *288*(5), 405–457.

Blackman, D. K., Ildefonse, B., John, B. E., Ohara, Y., Miller, D., Abe, N., Abratis, M., et al. (2011). Drilling constraints on lithospheric accretion and evolution at Atlantis Massif, Mid-Atlantic Ridge 30°N. *Journal of Geophysical Research*, *116*, BO7103. https://doi.org/10.1029/2010JB007931

Blackman, D. K., Ildefonse, B., John, B. E., Ohara, Y., Miller, D. J., MacLeod, C. J., & Scientists, A. T. E. (2006). Oceanic core complex formation, Atlantis Massif. *Proceedings of the Ocean Drilling Program*, *304/305*. https://doi.org/10.2204/iodp.proc.304305.2006

Blackman, D. K., Karson, J. A., Kelley, D. S., Cann, J. R., Früh-Green, G. L., Gee, J. S., et al. (2002). Geology of the Atlantis Massif (Mid-Atlantic Ridge, 30°N): Implications for the evolution of an ultramafic oceanic core complex. *Marine Geophysical Researches*, *23*(5/6), 443–469. https://doi.org/10.1023/B:MARI.0000018232.14085.75

Bonatti, E., Honnorez, J., & Ferrara, G. (1971). I. Ultramafic rocks-peridotite—gabbro—basalt complex from the equatorial Mid-Atlantic Ridge. *Philosophical Transactions of the Royal Society of London A*, *268*(1192), 385–402. https://doi.org/10.1098/rsta.1971.0002

Boschi, C., Früh-Green, G. L., Delacour, A., Karson, J. A., & Kelley, D. S. (2006). Mass transfer and fluid flow during detachment faulting and development of an oceanic core complex, Atlantis Massif (MAR 30°N). *Geochemistry, Geophysics, Geosystems*, *7*, Q01004. https://doi.org/10.1029/2005GC001074

Bronner, A., Sauter, D., Manatschal, G., Péron-Pinvidic, G., & Munschy, M. (2011). Magmatic breakup as an explanation for magnetic anomalies at magma-poor rifted margins. *Nature Geoscience*, *4*(8), 549–553. https://doi.org/10.1038/ngeo1201

Cannat, M., Karson, J., & Miller, D. (1995). *Proceedings of the Ocean Drilling Program, Part A: Initial Reports, 153*. College Station, TX: Ocean Drilling Program. https://doi.org/10.2973/odp.proc.ir.153.1995

Cannat, M., Manatschal, G., Sauter, D., & Peron-Pinvidic, G. (2009). Assessing the conditions of continental breakup at magma-poor rifted margins: What can we learn from slow spreading mid-ocean ridges? *Comptes Rendus Geoscience*, *341*(5), 406–427. https://doi.org/10.1016/j.crte.2009.01.005

Carlson, R. L., & Miller, D. J. (1997). A new assessment of the abundance of serpentinite in the oceanic crust. *Geophysical Research Letters*, *24*, 457–460. https://doi.org/10.1029/97GL00144

Carlson, R. L., & Miller, D. J. (2003). Mantle wedge water contents estimated from seismic velocities in partially serpentinized peridotites. *Geophysical Research Letters*, *30*(5), 1250. https://doi.org/10.1029/2002GL016600

Carlson, R. L., & Miller, J. D. (2004). Influence of pressure and mineralogy on seismic velocities in oceanic gabbros: Implications for the composition and state of the lower oceanic crust. *Journal of Geophysical Research*, *109*, B09205. https://doi.org/10.1029/2003JB002699

Christensen, N., Carlson, R., Salisbury, M., & Fountain, D. (1975). Elastic wave velocities in volcanic and plutonic rocks recovered on DSDP Leg 31. In D. E. Karig, et al. (Eds.), *Initial Reports of the Deep Sea Drilling Project* (Vol. XXXI, pp. 607–610). Washington, DC: U.S. Govt. Ptg. Ofc.

Christensen, N., Wepfer, W., & Baud, R. (1989). Seismic properties of sheeted dikes from Hole 504B, ODP Leg 1111. In *Proceedings of the Ocean Drilling Program, Scientific Results* (Vol. 111, pp. 171–176).

Christensen, N. I. (1966). Elasticity of ultrabasic rocks. *Journal of Geophysical Research*, *71*, 5921–5931. https://doi.org/10.1029/JZ071i024p05921

Christensen, N. I. (2004). Serpentinites, peridotites, and seismology. *International Geology Review*, *46*(9), 795–816. https://doi.org/10.2747/0020-6814.46.9.795

Cole, P., Minshull, T., & Whitmarsh, R. (2002). Azimuthal seismic anisotropy in a zone of exhumed continental mantle. *West Iberia margin, Geophysical Journal International*, *151*(2), 517–533. https://doi.org/10.1046/j.1365-246X.2002.01781.x

Dean, S., Minshull, T., Whitmarsh, R., & Louden, K. (2000). Deep structure of the ocean-continent transition in the southern Iberia Abyssal Plain from seismic refraction profiles: The IAM-9 transect at 40° 20′N. *Journal of Geophysical Research*, *105*, 5859–5885. https://doi.org/10.1029/1999JB900301

Escartín, J., & Cannat, M. (1999). Ultramafic exposures and the gravity signature of the lithosphere near the Fifteen-Twenty Fracture Zone (Mid-Atlantic Ridge, 14°–16.5°N). *Earth and Planetary Science Letters*, *171*(3), 411–424. https://doi.org/10.1016/S0012-821X(99)00169-7

Escartín, J., Mével, C., MacLeod, C. J., & McCaig, A. (2003). Constraints on deformation conditions and the origin of oceanic detachments: The Mid-Atlantic Ridge core complex at 15° 45′N. *Geochemistry, Geophysics, Geosystems*, *4*(8), 1067. https://doi.org/10.1029/2002GC000472

Evans, R. L., Escartín, J., & Cannat, M. (2010). A short electromagnetic profile across the Kane Oceanic Core Complex. *Geophysical Research Letters*, *37*, L15309. https://doi.org/10.1029/2010GL043813

Falcon-Suarez, I., Bayrakci, G., Minshull, T. A., North, L. J., Best, A. I., Rouméjon, S., & Party, I. E. S. (2017). Elastic and electrical properties and permeability of serpentinites from Atlantis Massif, Mid-Atlantic Ridge. *Geophysical Journal International*, *211*(2), 708–721.

Falcon-Suarez, I., North, L., Amalokwu, K., & Best, A. (2016). Integrated geophysical and hydromechanical assessment for CO2 storage: Shallow low permeable reservoir sandstones. *Geophysical Prospecting*, *64*(4), 828–847. https://doi.org/10.1111/1365-2478.12396

Früh-Green, G. L., Orcutt, B. N., Green, S., Cotterill, C., Morgan, S., Akizawa, N., et al. (2017). Expedition 357 summary. Proceedings of the International Ocean Discovery Program, Expedition Reports (Vol. 357). https://doi.org/10.14379/iodp.proc.357.101.2017

Früh-Green, G., Orcutt, B., Rouméjon, S., Lilley, M., Morono, Y., Cotterill, C., et al. (2018). Magmatism, serpentinization and life: Insights through drilling the Atlantis Massif (IODP Expedition 357).

Früh-Green, G. L., Kelley, D. S., Bernasconi, S. M., Karson, J. A., Ludwig, K. A., Butterfield, D. A., et al. (2003). 30,000 years of hydrothermal activity at the lost city vent field. *Science*, *301*(5632), 495–498. https://doi.org/10.1126/science.1085582.

Früh-Green, G. L., Orcutt, B. N., Green, S., Cotterill, C., & McCaig, A. (2016). Expedition 357 preliminary report: Atlantis Massif serpentinization and life. *International Ocean Discovery Program Preliminary reports*. https://doi.org/10.14379/iodp.pr.357.2016

Gillis, K., Snow, J., Klaus, A., Guerin, G., Abe, N., Akizawa, N., et al. (2013). Exploring the plutonic crust at a fast-spreading ridge: New drilling at Hess Deep, *Rep* Lawrence Livermore National Laboratory (LLNL), Livermore, CA.

Grimes, C. B., John, B. E., Cheadle, M. J., & Wooden, J. L. (2008). Protracted construction of gabbroic crust at a slow spreading ridge: Constraints from 206Pb/238U zircon ages from Atlantis Massif and IODP Hole U1309D (30°N, MAR). *Geochemistry, Geophysics, Geosystems*, *9*, Q08012. https://doi.org/10.1029/2008GC002063

Guéguen, Y., & Palciauskas, V. (1994). *Introduction to the physics of rocks*. Princeton, NJ: Princeton University Press.

Guo, X., Yoshino, T., & Katayama, I. (2011). Electrical conductivity anisotropy of deformed talc rocks and serpentinites at 3 GPa. *Physics of the Earth and Planetary Interiors*, *188*(1–2), 69–81. https://doi.org/10.1016/j.pepi.2011.06.012

Harding, A. J., Arnulf, A. F., & Blackman, D. K. (2016). Velocity structure near IODP Hole U1309D, Atlantis Massif, from waveform inversion of streamer data and borehole measurements. *Geochemistry, Geophysics, Geosystems*, *17*, 1990–2014. https://doi.org/10.1002/2016GC006312

Horen, H., Zamora, M., & Dubuisson, G. (1996). Seismic waves velocities and anisotropy in serpentinized peridotites from xigaze ophiolite: Abundance of serpentine in slow spreading ridge. *Geophysical Research Letters*, *23*, 9–12. https://doi.org/10.1029/95GL03594

Hyndman, R., & Drury, M. (1976). The physical properties of oceanic basement rocks from deep drilling on the Mid-Atlantic Ridge. *Journal of Geophysical Research*, *81*, 4042–4052. https://doi.org/10.1029/JB081i023p04042

Ildefonse, B., Blackman, D., John, B., Ohara, Y., Miller, D., & MacLeod, C. J. (2007). Oceanic core complexes and crustal accretion at slow-spreading ridges. *Geology*, *35*(7), 623–626. https://doi.org/10.1130/G23531A.1

Ildefonse, B., Drouin, M., Violay, M., & Pezard, P. (1997). Data report: Electrical properties of gabbroic and troctolitic rocks from IODP Hole U1309D, Atlantis Massif. Paper presented at Proc. IODP|Volume.

Ildefonse, B., & Pezard, P. (2001). Electrical properties of slow-spreading ridge gabbros from ODP Site 735. *Southwest Indian Ridge, Tectonophysics*, *330*(1–2), 69–92. https://doi.org/10.1016/S0040-1951(00)00220-1

Iturrino, G. J., Christensen, N. I., Kirby, S. H., Salisbury, M. H., Robinson, P. T., Adamson, A. C., et al. (1991). Seismic velocities and elastic properties of oceanic gabbroic rocks from Hole 735B. *Proceedings of the Ocean Drilling Program, Scientific Results*, *118*, 227–244. https://doi.org/10.2973/odp.proc.sr.118.151.1991

Iturrino, G. J., Miller, D. J., & Christensen, N. I. (1996). Velocity behavior of lower crustal and upper mantle rocks from a fast-spreading ridge at hess deep. In *Proceedings of the Ocean Drilling Program*, *Scientific Results* (Vol. 147, pp. 417–440). College Station, TX: Ocean Drilling Program.

Karson, J., & Dick, H. (1983). Tectonics of ridge-transform intersections at the Kane fracture zone. *Marine Geophysical Researches*, *6*(1), 51–98. https://doi.org/10.1007/BF00300398

Karson, J. A., Früh-Green, G., Kelley, D. S., Williams, E., Yoerger, D. R., & Jakuba, M. (2006). Detachment shear zone of the Atlantis Massif core complex, Mid-Atlantic Ridge, 30°N. *Geochemistry, Geophysics, Geosystems*, *7*, Q06016. https://doi.org/10.1029/2005GC001109

Katayama, I., Terada, T., Okazaki, K., & Tanikawa, W. (2012). Episodic tremor and slow slip potentially linked to permeability contrasts at the Moho. *Nature Geoscience*, *5*(10), 731–734. http://www.nature.com/ngeo/journal/v5/n10/abs/ngeo1559.html#supplementary-information

Kawano, S., Katayama, I., & Okazaki, K. (2011). Permeability anisotropy of serpentinite and fluid pathways in a subduction zone. *Geology*, *39*(10), 939–942. https://doi.org/10.1130/g32173.1

Kelemen, P. B., Kikawa, E., Miller, D. J., & Party, S. S. (2007). Leg 209 summary: Processes in a 20-km-thick conductive boundary layer beneath the Mid-Atlantic Ridge, 14–16°N. In *Proceedings of the Ocean Drilling Program*, *scientific results* (Vol. 209, pp. 1–33). College Station, TX: Ocean Drilling Program. https://doi.org/10.2973/odp.proc.sr.209.001.2007

Kelley, D. S., Karson, J. A., Früh-Green, G. L., Yoerger, D. R., Shank, T. M., Butterfield, D. A., et al. (2005). A serpentinite-hosted ecosystem: The Lost City hydrothermal field. *Science*, *307*(5714), 1428–1434. https://doi.org/10.1126/science.1102556

Kelley, D. S., Karson, J. A., Blackman, D. K., Früh-Green, G. L., Butterfield, D. A., Lilley, M. D., Olson, E. J., et al., & the AT3-60 Shipboard Party (2001). An off-axis hydrothermal vent field near the Mid-Atlantic Ridge at 30(deg) N. *Nature*, *412*(6843), 145–149. https://doi.org/10.1038/35084000

Kylander, O. S., & Kylander, K. (1999). Gimp the official handbook with Cdrom, coriolis value.

Lakio, S., Heinämäki, J., & Yliruusi, J. (2010). Colorful drying. *AAPS PharmSciTech*, *11*(1), 46–53. https://doi.org/10.1208/s12249-009-9351-x

Macdonald, A., & Fyfe, W. (1985). Rate of serpentinization in seafloor environments. *Tectonophysics*, *116*(1–2), 123–135. https://doi.org/10.1016/0040-1951(85)90225-2

MacLeod, C., Boudier, F., Yaouancq, G., & Richter, C. (1996). Gabbro fabrics from Site 894, Hess Deep: Implications for magma chamber processes at the East Pacific Rise. In *Proceedings of the Ocean Drilling Program*, *Scientific Results* (Vol. 147, pp. 317–328). College Station, TX: Ocean Drilling Program.

MacLeod, C., Célérier, B., Früh-Green, G., & Manning, C. (1996). Tectonics of Hess Deep: A synthesis of drilling results from Leg 147. In *Proceedings of the Ocean Drilling Program*, *Scientific Results* (Vol. 147, pp. 461–476). College Station, TX: Ocean Drilling Program.

Manning, C. E., & Ingebritsen, S. E. (1999). Permeability of the continental crust: Implications of geothermal data and metamorphic systems. *Reviews of Geophysics*, *37*, 127–150. https://doi.org/10.1029/1998RG900002

McCann, C., & Sothcott, J. (1992). Laboratory measurements of the seismic properties of sedimentary rocks. *Geological Society, London, Special Publications*, *65*(1), 285–297. https://doi.org/10.1144/gsl.sp.1992.065.01.22

Mével, C., & Stamoudi, C. (1996). Hydrothermal alteration of the upper-mantle section at Hess Deep1. *Proceeding of the Ocean Drilling Program, Scientific Results*, *147*. https://doi.org/10.2973/odp.proc.sr.147.017.1996

Miller, D. J., & Christensen, N. I. (1997). Seismic velocities of lower crustal and upper mantle rocks from the slow-spreading Mid-Atlantic Ridge, south of the Kane Transform Zone (MARK). In J. A. Karson, M. Cannat, D. J. Miller, & D. Elthon (Eds.), *Proc. ODP*, *Sci. Results* (Vol. 153, pp. 437–454). College Station, TX: Ocean drilling Program. https://doi.org/10.2973/odp.proc.sr.153.043.1997

Minshull, T. A. (2009). Geophysical characterisation of the ocean–continent transition at magma-poor rifted margins. *Comptes Rendus Geoscience*, *341*(5), 382–393. https://doi.org/10.1016/j.crte.2008.09.003

Morris, A., Gee, J., Pressling, N., John, B., MacLeod, C. J., Grimes, C., & Searle, R. (2009). Footwall rotation in an oceanic core complex quantified using reoriented Integrated Ocean Drilling Program core samples. *Earth and Planetary Science Letters*, *287*(1–2), 217–228. https://doi.org/10.1016/j.epsl.2009.08.007

North, L., Best, A. I., Sothcott, J., & MacGregor, L. (2013). Laboratory determination of the full electrical resistivity tensor of heterogeneous carbonate rocks at elevated pressures. *Geophysical Prospecting*, *61*(2), 458–470. https://doi.org/10.1111/j.1365-2478.2012.01113.x

North, L. J., & Best, A. I. (2014). Anomalous electrical resistivity anisotropy in clean reservoir sandstones. *Geophysical Prospecting*, *62*(6), 1315–1326. https://doi.org/10.1111/1365-2478.12183

Pressling, N., Morris, A., John, B. E., & MacLeod, C. J. (2012). The internal structure of an oceanic core complex: An integrated analysis of oriented borehole imagery from IODP Hole U1309D (Atlantis Massif). *Geochemistry, Geophysics, Geosystems*, *13*, Q04G10. https://doi.org/10.1029/2012GC004061

Rasband, W. (1997). ImageJ software, National Institutes of Health: Bethesda, MD, USA, 2012.

Rouméjon, S., & Cannat, M. (2014). Serpentinization of mantle-derived peridotites at mid-ocean ridges: Mesh texture development in the context of tectonic exhumation. *Geochemistry, Geophysics, Geosystems*, *15*, 2354–2379. https://doi.org/10.1002/2013GC005148

Rouméjon, S., Früh-Green, G. L., Orcutt, B. N., & the IODP Expedition 357 Science Party (2018). Alteration heterogeneities in peridotites exhumed on the southern wall of the Atlantis Massif (IODP Expedition 357). *Journal of Petrology*, 1–29. https://doi.org/10.1093/petrology/egy065

Rüpke, L. H., Schmid, D. W., Perez-Gussinye, M., & Hartz, E. (2013). Interrelation between rifting, faulting, sedimentation, and mantle serpentinization during continental margin formation—including examples from the Norwegian Sea. *Geochemistry, Geophysics, Geosystems*, *14*, 4351–4369. https://doi.org/10.1002/ggge.20268

Sauter, D., Cannat, M., Rouméjon, S., Andreani, M., Birot, D., Bronner, A., Brunelli, D., et al. (2013). Continuous exhumation of mantle-derived rocks at the Southwest Indian Ridge for 11 million years. *Nature Geoscience*, *6*(4), 314–320. https://doi.org/10.1038/ngeo1771

Schroeder, T., & John, B. E. (2004). Strain localization on an oceanic detachment fault system, Atlantis Massif, 30°N, Mid-Atlantic Ridge. *Geochemistry, Geophysics, Geosystems*, *5*, 011007. https://doi.org/10.1029/2004GC000728

Sibuet, J. C., Srivastava, S., & Manatschal, G. (2007). Exhumed mantle-forming transitional crust in the Newfoundland-Iberia rift and associated magnetic anomalies. *Journal of Geophysical Research*, *112*, B06105. https://doi.org/10.1029/2005JB003856

Stesky, R. M., & Brace, W. F. (1973). Electrical conductivity of serpentinized rocks to 6 kilobars. *Journal of Geophysical Research*, *78*, 7614–7621. https://doi.org/10.1029/JB078i032p07614

Toft, P. B., Arkani-Hamed, J., & Haggerty, S. E. (1990). The effects of serpentinization on density and magnetic susceptibility: A petrophysical model. *Physics of the Earth and Planetary Interiors*, *65*(1–2), 137–157. https://doi.org/10.1016/0031-9201(90)90082-9

Trimmer, D., Bonner, B., Heard, H., & Duba, A. (1980). Effect of pressure and stress on water transport in intact and fractured gabbro and granite. *Journal of Geophysical Research*, *85*, 7059–7071. https://doi.org/10.1029/JB085iB12p07059

Tucholke, B. E., & Lin, J. (1994). A geological model for the structure of ridge segments in slow spreading ocean crust. *Journal of Geophysical Research*, *99*, 11,937–11,958. https://doi.org/10.1029/94JB00338

Tucholke, B. E., & Sibuet, J.-C. (2007). Leg 210 synthesis: Tectonic, magmatic, and sedimentary evolution of the Newfoundland-Iberia rift. In *Proceedings of the Ocean Drilling Program*, *Scientific Results* (Vol. 210, pp. 1–56). College Station, TX: Ocean Drilling Program.

Yaouancq, G., & MacLeod, C. J. (2000). Petrofabric investigation of gabbros from the Oman ophiolite: Comparison between AMS and rock fabric. *Marine Geophysical Research*, *21*(3/4), 289–306. https://doi.org/10.1023/A:1026774111021

Zervas, C. E., Sempéré, J.-C., & Lin, J. (1995). Morphology and crustal structure of a small transform fault along the Mid-Atlantic Ridge: The Atlantis Fracture Zone. *Marine Geophysical Researches*, *17*(3), 275–300. https://doi.org/10.1007/BF01203466